https://doi.org/10.1016/j.jsv.2018.04.034

Thermo-acoustics generated by periodically heated thin line array

Y.S. Liu[a], L.H. Tong[b,*], S.K. Lai[c,d]

[a] Institute of Engineering Mechanics, School of Civil Engineering and Architecture, East China Jiaotong University, Nanchang, Jiangxi, P.R. China

[b] Jiangxi Key Laboratory of Infrastructure Safety and Control in Geotechnical Engineering, East China Jiaotong University, Nanchang, Jiangxi, P.R. China

[c] Department of Civil and Environmental Engineering, The Hong Kong Polytechnic University, Hung Hom, Kowloon, Hong Kong, P.R. China

[d] The Hong Kong Polytechnic University Shenzhen Research Institute, Shenzhen, P.R. China

[*]Corresponding author. E-mail: lhtong@ecjtu.edu.cn

Abstract

A theoretical model for the generation of thermo-acoustic waves from a heated point source in a free-space and a half-space is proposed, where the source is suspended over a substrate. By directly applying the analytical results of a point source to a thin line thermo-acoustic speaker, the acoustic pressure field generated by the periodically heated thin line can be derived using a mathematical integration technique. To further generalize the results from a thin line speaker to a thin line array, the acoustic pressure response generated by the line array speaker can also be implemented in both free- and half-spaces. In this work, the characteristics of pressure fields generated by the thin line array are investigated in detail. The established model is well validated by comparing with the existing experimental results. The present findings not only can be extended to investigate thermo-acoustic responses generated by arbitrary sources, and also it can provide important design guidelines for the manipulation and optimization of thin line array thermo-acoustic devices.

Keywords: Thermo-acoustics; Carbon nanotube yarn; Line array transduction

1. Introduction

Thermo-acoustic (TA) transducers have attracted more research attention in recent years due to their superior properties of light weight and broadband response. The generation mechanism of TA devices is completely different with that of conventional mechanically driven loudspeakers. On the basis of this thermal principle, acoustic waves can be efficiently generated from the expansion and contraction of a medium that is heated periodically by applying an alternating current on a thin conductor [1]. However, the development of TA devices has remained stagnant for more than eighty years since it was first introduced by Arnold and Crandall [2], which is mainly attributed to the lack of innovative technology on the fabrication of smart materials. With the advancement of nanomaterials and nanotechnology at a rapid pace, it sheds light on the breakthrough technology of TA devices. The first efficient thermal ultrasound emitter was proposed by Shinoda et al. [3] in 1999, in which a patterned thin aluminum film was directly placed on a microporous silicon layer to serve as a major component for sound geenration. An improved electrical power to sound power conversion efficiency was demostrated by the experimental observation, which is beneficial from the low heat capacity per unit area (HCPUA) of a 30-nm aluminum film used as a thermal ultrasound emitter. To compare with conventional mechanically driven speakers, the conversion efficiency is still low due to the significant thermal leakage into the substrate. Nervertheless, it has been demonstrated that TA transducers can exhibit broadband responses, but conventional loudspeakers do not possess this feature [4]. Hence, it is highly desired to explore potential applications in the technological development of TA loudspeakers and transducers [5].

To enhance the conversion efficiency of TA devices, Xiao and his co-workers [6] proposed a newly-fabricated carbon nanotube (CNT) thinfilm [7, 8], which can be drawn from nano-materials composed of a super-aligned CNT array as a thermal source. CNT thinfilms are able to generate considerable acoustic signals by feeding an alternating current onto it [6]. The high electrical power to sound power conversion efficiency of CNT thinfilm TA devices is mainly come from two sides. One is from its extremely small HCPUA and the other one is due to the suspension structure. Unlike the TA device designed by Shinoda et al. [3], a non-substrated structure TA transducer introduced by Xiao et al.[6] enables most of the thermal energy to heat the surrounding medium (fluidic or gaseous medium), resulting in a higher energy conversion. In pursuit of alternative forms, multiple types of TA devices were subsequently reported, including CNT assemblies [9], metallic wire arrays and metallic thinfilms [10-14], graphene-on-paper [15], CNT yarn array suspended on a substrate [5], carbon fiber array encapulated in a planar enclosure [16], carbonized electrospun nanofiber sheets [17] and even individual CNTs [18, 19].

In the literature, the performance of TA devices in both gaseous and fluidic media was extensively investigated. Aliev et al. [20] reported an experimental study for the investigation of TA responses in water, ethanol and methanol. A higher pressure in water can be produced due to the hydrophobicity of the CNT sheets. In addition, Xiao et al.[21]

and Aliev et al.[22] also investigated the performance of TA devices immersed in various gaseous media for the frequency spectrum analysis of TA signals. They found that there is a dominant effect for the thermal properties of surrounding gaseous media on the generation of acoustic pressure fields. In addition, the experimental results also showed that the performance of TA devices is completely different in closed systems and open spaces.

Nevertheless, there are few theoretical works attempted on the investigation of TA responses. Hu et al.[23] considered a set of coupled thermal-mechanical equations to study the ultrasound effect generated by an aluminum-porous silicon TA device. Xiao et al. [6] constructed a piston model to explain the importance of the HCPUA on the thermal-acoustic generation efficiency. To improve the piston model of Xiao et al.[6], an accurate analytical model was proposed by Lim et al.[24] to show an excellent agreement with the experimental results. Besides, Vesterinen et al. [11] theoretically investigated the efficiency of TA devices made of aluminum wire arrays. The influence of the appearance of substrates on the generation of acoustic waves was also demonstrated. Asadzadeh et al. [25] derived a formula for sound generation of small TA sound sources using two alternative forms of energy in terms of energy conducted to the fluid. To study acoustic pressure in the near-field region, a 3-dimensional governing equation was formulated and solved using the finite difference method. Tong and his associates [26, 27] constructed two theoretical models to study the acoustic fields generated by specific types of TA devices, i.e., encapsulated TA transducers and gap-separation TA devices. Subsequently, acoustic field responses to various broadband input signals applied to both free-standing and nano-thinfilm-substrate TA devices were also investigated [4]. More recently, an electrical-thermal-acoustical model was constructed by Asgarisabet and Barnard [28] for the simulation of pressure distribution in an open medium by feeding an electric current into a CNT film. The influence of material properties in the surrounding medium on the output sound pressure was also discussed.

Although an industrial revolution in the fabrication of nanomaterials has significantly advanced the technology of TA devices to improve our daily audio experience, the weak structure form of free-standing CNT sheets [5] and the low energy conversion efficiency of film-substrate structures are still difficult to realize its practical applications. Consider the fascinating and promising applications of thin nano-structures on the design of TA devices, an improvement on the structure strength is highly demanded. Wei et al.[5] took advantage of the high mechanical strength of CNT thin line array to manufacture a suspended TA device, which can tactfully solve the weak structure problem involved in fresh CNT films. As the thin line array is suspended over a silicon substrate with a gap separation that can efficiently reduce the thermal leakage into the substrate, leading to a higher efficiency. However, Wei et al. [5] only presented a qualitative analysis on the experimental observation according to the model proposed by Xiao et al. [6]. Based on the previous study [5], Tong et al. [27] further developed an accurate approximate model to account for the acoustic pressure response of nano-film-substrate TA devices. In order to substantially investigate the performance of TA effect, a rigorous theoretical model is greatly desired for further design and optimization of thin line array TA devices.

Presented herein is a rigorous model to investigate the acoustic pressure response of thin line TA devices. Consider that receiving points are mostly within the far-field region, acoustic pressure responses in the far-field region are of great interest and thus it is the major scope of the present work. Both frequency- and power-dependent pressure responses are compared with the available experimental results to validate the accuracy of this analytical model. The characteristics of pressure distribution in a semi-space are also investigated. By increasing frequency results in the appearance of the principal maxima and the side-lobes due to the strong interference effect. Furthermore, a phased array TA emission by feeding an alternating current with different phase shifts onto the TA device is studied. The characteristics of the angular distribution of acoustic pressure is also presented.

2. Theory and analytical models

Consider a thin line array TA device that is made of a series of parallel thin lines as shown in Fig. 1. By superposing all acoustic pressure fields generated by these thin lines, we can obtain a total acoustic pressure field produced by the thin line array TA device. Prior to evaluating the acoustic pressure response of a thin line pattern, it is important to understand the nature of this structure. Obviously, a thin line source can be regarded as finite and continuous point sources aligned along the length direction of the line. Hence, the emission of acoustic waves from a point source in an open space will be studied first in the subsequent sections.

2.1 Temperature fields generated by a point source

In the first situation, i.e., a source point in an open space, the coupled thermal field equation under the assumption of non-viscous and linear conditions is [11, 29]

$$\nabla^2 T - \frac{1}{\alpha}\frac{\partial T}{\partial t} = -\frac{1}{\kappa}\frac{\partial p}{\partial t} - \frac{S}{\kappa} \tag{1}$$

where ∇^2 is the Laplace operator, T is the varying temperature, α is the thermal diffusivity of medium, κ is the heat conductivity of medium, S is the heat source with unit of $\mathrm{W/m^3}$, p is the sound pressure and t is time. Suppose that the point source is set at the coordinate $(0, 0, \mathrm{g})$ and it is expressed as $S = P_{in}^{e} \cdot \delta(x)\delta(y)\delta(z-g)e^{-\mathrm{j}\omega t}$ with ω the circular frequency, $\delta(\cdot)$ the Dirac delta function and $\mathrm{j} = \sqrt{-1}$. It is noted that P_{in}^{e} is the effective input power that is only part of the total input power when we consider the effect of heat loss. As the contribution from the variation of acoustic pressure fields to temperature is insignificant within low frequency range (less than 100 kHz), so we can ignore this factor [11]. Assume that the time-dependent term of the temperature field T is $\mathrm{e}^{-\mathrm{j}\omega t}$, then Eq.(1) can be re-written as

$$\nabla^2 \overline{T} + \lambda^2 \overline{T} = -\frac{P_{in}^{e}}{\kappa}\delta(x)\delta(y)\delta(z-g) \tag{2}$$

where $\lambda = \sqrt{\mathrm{j}\omega/\alpha} = \sqrt{\omega/(2\alpha)} + \mathrm{j}\sqrt{\omega/(2\alpha)}$ and $\overline{T}$ satisfies the condition

$T = \overline{T} \cdot \mathrm{e}^{-\mathrm{j}\omega t}$. By using the Green function method [30], the solution to Eq.(2) can be obtained as

$$\overline{T}(\vec{r}, g) = -\frac{P_{in}^{e}}{4\pi\kappa} \frac{e^{j\lambda|\vec{r}-g\vec{\mathrm{e}}_z|}}{|\vec{r}-g\vec{\mathrm{e}}_z|} \tag{3}$$

where $\vec{r}$ is a vector from the origin to (x, y, z) and $\vec{\mathrm{e}}_z$ is a unit vector along the z-direction.

While for the second situation, i.e., a substrate is placed on the surface $z = 0$, the thermal properties of the substrate have significant influence on the temperature field generated by the point source due to the thermal leakage into the substrate [27]. In order to find the temperature distribution $T_g(\vec{r}, g; t)$ and satisfy Eq. (2) for this situation, the complex equivalent source method proposed by Ochmann [31] is employed. The subscript g denotes the quantity related to the second situation. A key point to use this method is to determine the boundary condition at the surface $z = 0$. If the surface temperature of the substrate at $z = 0$ is $T_0(x, \mathrm{y}; \mathrm{t}) = \overline{T}_g(\vec{r}, g)\big|_{z=0} \cdot \mathrm{e}^{-\mathrm{j}\omega t}$, we assume that the thermal waves in the substrate only propagate along the negative z-direction. Hence, the thermal waves in the substrate can be expressed as $T_s(\vec{r}; t) = T_0(x, \mathrm{y}; \mathrm{t}) \cdot \mathrm{e}^{-\mathrm{j}\lambda_s z}$, in which $\lambda_s = \sqrt{\mathrm{j}\omega/\alpha_s}$ and α_s is the thermal diffusivity of the substrate. Consider that the decay of the thermal waves is neglected within one wavelength $\delta_s = 2\pi\sqrt{2\alpha_s/\omega}$, so the average temperature rise of the substrate can be estimated by the following equation

$$T_{s,t} = \frac{1}{\delta_s}\int_{-\delta_s}^{0} T_0(x, \mathrm{y}; \mathrm{t}) \cdot e^{-\mathrm{j}\lambda_s z} dz = \frac{\mathrm{j}\left(1 - e^{\mathrm{j}\lambda_s \delta_s}\right)}{\delta_s \lambda_s} \overline{T}_g(\vec{r}, g)\big|_{z=0} \mathrm{e}^{-\mathrm{j}\omega t} \tag{4}$$

Omitting the heat loss by radiation and convection at the surface $z = 0$ and following the conservation of energy, we have

$$\kappa \frac{\partial T_g(\vec{r},g;t)}{\partial z} = \delta_s C_{Vs} \frac{\partial T_{s,t}}{\partial t} \quad \text{at } z=0 \tag{5}$$

where C_{Vs} is the heat capacity of the substrate with unit of J/(m^3 K). Making use of Eqs. (4) and (5) yields the boundary condition at $z = 0$ as

$$\frac{\partial \overline{T}_g(\vec{r},g)}{\partial z} + \varepsilon \overline{T}_g(\vec{r},g;t) = 0 \quad \text{at } z=0 \tag{6}$$

where $\varepsilon = \omega C_{Vs}\left(e^{\mathrm{j}\lambda_s\delta_s}-1\right)/\left(\kappa\lambda_s\right)$. The solution to Eq. (2) under the boundary condition in Eq. (6) can be directly obtained using the complex equivalent source method [31] as

$$\overline{T}_g(\vec{r},g) = \overline{T}(\vec{r},g) + \overline{T}(\vec{r},-g) + 2\mathrm{j}\varepsilon\int_{-\infty}^{0} \overline{T}(\vec{r},-g+j\varsigma)e^{-\mathrm{j}\varepsilon\varsigma}\mathrm{d}\varsigma \tag{7}$$

2.2 Acoustic fields generated by a point heat source

The variation of temperature in a surrounding medium can cause the expansion and contraction of the medium to generate acoustic waves. The coupled equation is given by [27]

$$\nabla^2 P - \frac{1}{C_0^2}\frac{\partial^2 P}{\partial t^2} = -\frac{\alpha}{\kappa}\frac{\rho_0}{T_0}\frac{\partial\left(\kappa\nabla^2 T + S\right)}{\partial t} \tag{8}$$

where P is the variation of acoustic pressure.

Consider acoustic pressure fields generated by a heat point source in a free space, we substitute Eq. (3) into Eq. (8) and set $g = 0$ for simplification to obtain

$$\nabla^2 \overline{P}(\vec{r}) + k^2 \overline{P}(\vec{r}) = \frac{\rho_0\omega^2}{T_0}\frac{P_{in}^{\ e}}{4\pi\kappa}\frac{e^{\mathrm{j}\lambda|\vec{r}|}}{|\vec{r}|} \tag{9}$$

where $P(\vec{r})=\overline{P}(\vec{r})\mathrm{e}^{-\mathrm{j}\omega t}$, $k=\omega/C_0$ is the wavenumber, C_0 is the isentropic sound speed, and $1/T_0$ is the volume coefficient of the thermal expansion for an ideal gas. Given that there is no reflection boundary condition in a free space, the solution to Eq. (9) is

$$\overline{P}(\vec{r})=\frac{D}{|\vec{r}|}e^{\mathrm{j}k|\vec{r}|}+\frac{\rho_0\omega^2}{T_0}\frac{P_{in}^{\ e}}{4\pi\kappa}\frac{1}{k^2-\lambda^2}\frac{e^{\mathrm{j}\lambda|\vec{r}|}}{|\vec{r}|} \tag{10}$$

where D is an undetermined coefficient. Assume the source is to be rigid, then we have the boundary condition $\mathrm{d}P/\mathrm{d}r\big|_{r\to 0}=0$. Substituting Eq. (10) into this boundary condition yields

$$D=\frac{\gamma-1}{\alpha}\frac{k^2}{k^2-\lambda^2}\frac{P_{in}^{\ e}}{4\pi} \tag{11}$$

where γ is the heat capacity ratio of gas. Here, we use the relationship $\rho_0\alpha/(\kappa T_0)=(\gamma-1)/C_0^{\ 2}$. Consider the particular solution term in Eq. (10), it is sharply attenuated within an extremely short distance, it can thus be neglected. As a result, the acoustic pressure solution can be simplified as

$$\overline{P}(\vec{r})=\frac{\gamma-1}{\alpha}\frac{k^2}{k^2-\lambda^2}\frac{P_{in}^{\ e}}{4\pi}\frac{e^{\mathrm{j}k|\vec{r}|}}{|\vec{r}|} \tag{12}$$

In the second situation, the corresponding coupled equation can be directly expressed by replacing $T(\vec{r};t)$ and $P(\vec{r};t)$ with $T_g(\vec{r},\mathrm{g};t)$ and $P_g(\vec{r},\mathrm{g};t)$, respectively in Eq. (8) as

$$\nabla^2\overline{P}_g(\vec{r},g)+k^2\overline{P}_g(\vec{r},g)=\frac{\rho_0\omega^2}{T_0}\overline{T}_g(\vec{r},g) \tag{13}$$

Due to the complexity of $\overline{T}_g(\vec{r},\mathrm{g})$, it is difficult to solve Eq. (13) with a direct method.

To seek the solution to Eq. (13), the method of Green's functions is used. The following equation represents the acoustic pressure field in a half space

$$\nabla^2 G_P\left(\vec{r},g\right)+k^2 G_P\left(\vec{r},g\right)=-\delta\left(x\right)\delta\left(y\right)\delta\left(z-g\right) \tag{14}$$

Applying the Green's function, the solution to Eq. (14) is obtained as [30]

$$G_P\left(\vec{r},g\right)=\frac{e^{\mathrm{j}k\left|\vec{r}-g\vec{\mathrm{e}}_z\right|}}{4\pi\left|\vec{r}-g\vec{\mathrm{e}}_z\right|}+\frac{e^{\mathrm{j}k\left|\vec{r}+g\vec{\mathrm{e}}_z\right|}}{4\pi\left|\vec{r}+g\vec{\mathrm{e}}_z\right|} \tag{15}$$

Then, the acoustic pressure field can be expressed in terms of a convolution integral [32] as

$$\overline{P}_g\left(\vec{r},g\right)=\frac{\rho_0\omega^2}{T_0}\int_{z'\geq 0} G_P\left(\vec{r}-\vec{r}',g\right)\overline{T}_g\left(\vec{r}',g\right)\mathrm{d}\vec{r}' \tag{16}$$

Although the integral domain is a half space, the influence range of $\overline{T}_g\left(\vec{r}',g\right)$ is only within one wavelength. In addition, observation points frequently are in the far-field region for practical consideration, thus the term $G_P\left(\vec{r}-\vec{r}',g\right)$ can be approximately equal to $G_P\left(\vec{r},g\right)$. This can safely move out of the integral without causing significant errors. To calculate the integral $\int_{z'\geq 0}\overline{T}_g\left(\vec{r}',g\right)\mathrm{d}\vec{r}'$, we transfer the rectangular coordinate into the spherical coordinate, i.e., $\left(x',y',z'-g\right)\mapsto\left(q,\theta,\varphi\right)$, with $q=\sqrt{x'^2+y'^2+\left(z'-g\right)^2}$, then $\overline{T}\left(\vec{r}',g\right)\mapsto\left(-P_{in}^{\,e}/\kappa\right)e^{j\lambda q}/\left(4\pi q\right)$. The integral $\int_{z'\geq 0}\overline{T}_g\left(\vec{r}',g\right)\mathrm{d}\vec{r}'$ can be easily solved as [32]

$$\int_{z'\geq 0}\overline{T}_g\left(\vec{r}',g\right)\mathrm{d}\vec{r}'=-\frac{P_{in}^{\,e}}{\kappa}\frac{1}{2k_T^{\,2}}\left(\mathrm{j}-\frac{\varepsilon\mathrm{e}^{(\mathrm{j}-1)k_T g}}{k_T+\mathrm{j}\left(k_T-\varepsilon\right)}\right) \tag{17}$$

where $k_T=\sqrt{\omega/\left(2\alpha\right)}$. The pressure field can be explicitly expressed as

$$\overline{P}_g\left(\vec{r},g\right)=-P_{in}^{\,e}\frac{\left(\gamma-1\right)\omega}{C_0^{\,2}}\left(\frac{e^{\mathrm{j}k\left|\vec{r}-g\vec{\mathrm{e}}_z\right|}}{4\pi\left|\vec{r}-g\vec{\mathrm{e}}_z\right|}+\frac{e^{\mathrm{j}k\left|\vec{r}+g\vec{\mathrm{e}}_z\right|}}{4\pi\left|\vec{r}+g\vec{\mathrm{e}}_z\right|}\right)\left(\mathrm{j}-\frac{\varepsilon\mathrm{e}^{(\mathrm{j}-1)k_T g}}{k_T+\mathrm{j}\left(k_T-\varepsilon\right)}\right) \tag{18}$$

From the second factor on the right-hand side of Eq. (18), there are two parts included. The first part is originated from the original source while the second one is contributed by the image source. In addition, the appearance of the last factor on the right-hand side of Eq. (18) is attributed to the substrate. The influence of the substrate on acoustic pressure fields is completely dominated by this factor.

2.3 Pressure fields generated by a line source

In this section, we consider acoustic pressure fields generated by a line source in a free space and a half space, as shown in Fig. 2. The pressure fields for both cases are separately investigated.

For the first scenario, i.e., a line source is located in a free-space, the coordinate geometry is shown in Fig. 2(a). The length of the line source is l that is greatly larger than its dimension in diameter. The efficient input power per unit length is P_{in}^{e}/l. The pressure field generated by a micro-element dy can be directly obtained from Eq. (12) as

$$\mathrm{d}\bar{P}(\vec{r}') = \frac{\gamma-1}{\alpha}\frac{k^2}{k^2-\lambda^2}\frac{P_{in}^{e}}{4\pi l}\frac{\mathrm{e}^{\mathrm{j}k|\vec{r}'|}}{|\vec{r}'|}\mathrm{d}y \tag{19}$$

The total pressure field generated by the line source can be obtained by integrating over the range $(-l/2, l/2)$ as

$$\bar{P}_L(\vec{r}') = \int_{-\frac{l}{2}}^{\frac{l}{2}}\frac{\gamma-1}{\alpha}\frac{k^2}{k^2-\lambda^2}\frac{P_{in}^{e}}{4\pi l}\frac{e^{\mathrm{j}k|\vec{r}'|}}{|\vec{r}'|}\mathrm{d}y \tag{20}$$

As the pressure in the far-field is of great interest, we consider the approximation

$|\vec{r}'| \approx |\vec{r}| - y\sin\theta$ and substitute this approximation into Eq. (20) to give the pressure field [33]

$$\bar{P}_L(\vec{r}) = -\mathrm{j}\frac{\gamma-1}{\alpha}\frac{k^2}{k^2-\lambda^2}\frac{P_{in}^{\ e}}{4\pi}\frac{\mathrm{e}^{\mathrm{j}k|\vec{r}|}}{|\vec{r}|}D_L(\theta) \tag{21}$$

where $D_L(\theta) = \mathrm{sinc}(kl\sin\theta/2)$ is the directional function of the line source. For this solution, the approximation $1/|\vec{r}'| = 1/(|\vec{r}| - y\sin\theta) \approx 1/|\vec{r}|$ is used for the condition $|\vec{r}| \gg |y\sin\theta|$ in the far-field region.

For a line source suspended over a substrate, i.e., a half-space problem, similar procedures can be used to obtain the corresponding pressure field. The coordinate arrangement is presented in Fig. 2 (b). The pressure field generated by a micro-element is written as

$$d\bar{P}_g(\vec{r},g) = \frac{P_{in}^{\ e}}{l}\frac{(\gamma-1)\omega}{C_0^{\ 2}}\left(\frac{\mathrm{e}^{\mathrm{j}k|\vec{r}'-g\vec{\mathrm{e}}_z|}}{4\pi|\vec{r}'-g\vec{\mathrm{e}}_z|} + \frac{\mathrm{e}^{\mathrm{j}k|\vec{r}'+g\vec{\mathrm{e}}_z|}}{4\pi|\vec{r}'+g\vec{\mathrm{e}}_z|}\right)\left(\mathrm{j} - \frac{\varepsilon\mathrm{e}^{(\mathrm{j}-1)k_T g}}{k_T + \mathrm{j}(k_T-\varepsilon)}\right)\mathrm{d}y \tag{22}$$

By using the approximations $|\vec{r}' - g\vec{\mathbf{e}}_z| \approx |\vec{r}| - g\sin\theta - y\sin\theta_o$ and $|\vec{r}' + g\vec{\mathbf{e}}_z| \approx |\vec{r}| + g\sin\theta_I - y\sin\theta_I$, we integrate Eq. (22) over the range $(-l/2, l/2)$ along the y-direction to achieve the following equation

$$\bar{P}_{gL}(\vec{r},g) = \frac{P_{in}^{\ e}}{4\pi}\frac{(\gamma-1)\omega}{C_0^{\ 2}}\left(1 + \frac{\mathrm{j}\varepsilon\mathrm{e}^{(\mathrm{j}-1)k_T g}}{k_T + j(k_T-\varepsilon)}\right)\left(\frac{\mathrm{e}^{\mathrm{j}k(|\vec{r}|-g\cos\theta)}}{|\vec{r}|-g\cos\theta}D_L(\theta_o) + \frac{\mathrm{e}^{\mathrm{j}k(|\vec{r}|+g\cos\theta_I)}}{|\vec{r}|+g\cos\theta_I}D_L(\theta_I)\right) \tag{23}$$

where θ_o and θ_I are defined in Fig. 2(b). They satisfy the conditions $\sin\theta_o \approx (|\vec{r}|\sin\theta)/(|\vec{r}| - g\cos\theta)$ and $\sin\theta_I \approx (|\vec{r}|\sin\theta)/(|\vec{r}| + g\cos\theta)$. Besides, the approximations in the far-field $1/|\vec{r}' - g\vec{\mathbf{e}}_z| \approx 1/(|\vec{r}| - g\sin\theta)$ and $1/|\vec{r}' - g\vec{\mathbf{e}}_z| \approx 1/(|\vec{r}| - g\sin\theta_I)$ are used to formulate Eq. (23).

2.4 Pressure fields generated by a line array

A thin line array TA device is composed a set of lines. Hence, the total pressure field generated by a thin line array TA device can be reached by adding all the pressure fields of those line sources together. There are two cases, namely (i) in a free space and (ii) in a half space, for a line array suspending over a substrate. The coordinate geometries for both cases are depicted in Fig. 3. Suppose that there are n lines with a pitch d in an array and the origin is located at the center of the array in case (a) and at the center of projection of the array on the substrate in case (b).

In case (a), the approximation $\left|\vec{r}_{iy}\right| \approx \left|\vec{r}\right| - (n+1)d/2 \cdot \sin\theta\cos\varphi - y\sin\theta\sin\varphi$ can be obtained, where $\theta = \langle \vec{z}, \vec{r} \rangle$ is from $\vec{z}$ to $\vec{r}$ and $\varphi = \left\langle \vec{x}, \overrightarrow{\mathrm{OP}}_j \right\rangle$ is from $\vec{x}$ to $\overrightarrow{\mathrm{OP}}_j$, see Fig. 3 (a). Suppose that the phase difference between two adjacent lines is $\Delta\psi$ and the phase shift of the i^{th} line relative to the first line is $(i-1)\Delta\psi$, then the pressure field can be expressed as [33]

$$\begin{aligned} \bar{P}_{LA}(\vec{r}) &= \sum_{i=1}^{n} \frac{\gamma-1}{\alpha} \frac{k^2}{k^2-\lambda^2} \frac{P_{in}^{e}}{4\pi n l} \int_{-l/2}^{l/2} \frac{\mathrm{e}^{\mathrm{j}\left[k\left|\vec{r}_{iy}\right| + (i-1)\Delta\psi\right]}}{\left|\vec{r}_{iy}\right|} \mathrm{d}y \\ &\approx \frac{\gamma-1}{\alpha} \frac{k^2}{k^2-\lambda^2} \frac{P_{in}^{e}}{4\pi} \frac{\mathrm{e}^{\mathrm{j}\left(k\left|\vec{r}\right| + \frac{n-1}{2}\Delta\psi\right)}}{\left|\vec{r}\right|} D_{LA}(\theta,\varphi,\Delta\psi) \end{aligned} \tag{24}$$

where $D_{LA}(\theta,\varphi,\Delta\psi) = \mathrm{sinc}\left(\frac{kl\sin\theta\sin\varphi}{2}\right) \frac{\sin\frac{n(kd\sin\theta\cos\varphi + \Delta\psi)}{2}}{n\sin\frac{kd\sin\theta\cos\varphi + \Delta\psi}{2}}$. When $n \to \infty$, $d \to 0$ and $\Delta\psi = 0$, the pressure field in Eq.(24) that is generated by a thinfilm can be expressed as

$$\bar{P}_f(\vec{r}) = \frac{\gamma-1}{\alpha}\frac{k^2}{k^2-\lambda^2}\frac{P_{in}^{e}}{4\pi}\frac{e^{j(k|\vec{r}|)}}{|\vec{r}|}D_f(\theta,\varphi) \tag{25}$$

where $D_f(\theta,\varphi) = \mathrm{sinc}(kl\sin\theta\sin\varphi/2)\mathrm{sinc}(kw\sin\theta\cos\varphi/2)$ with w the width of the thinfilm.

In case (b), the line array is located on the surface $z = g$. $\vec{r}$, $\vec{r}'$ and $\vec{r}''$ denote the vectors from the origin, (0,0,g) and (0,0,-g) to the observation point, respectively. It is easy to get the approximations $|\vec{r}'| \approx |\vec{r}| - g\cos\theta$ and $|\vec{r}''| \approx |\vec{r}| + g\cos\theta$. Using the same mathematical procedures to Eq. (24) with Eq. (23), the pressure field for this case is derived as [33]

$$\bar{P}_{gLA}(\vec{r},g) = \frac{P_{in}^{e}}{4\pi}\frac{(\gamma-1)\omega}{C_0^2}\left(1+\frac{\mathrm{j}\varepsilon e^{(\mathrm{j}-1)k_T g}}{k_T+\mathrm{j}(k_T-\varepsilon)}\right)\left(\frac{e^{\mathrm{j}k(|\vec{r}|-g\cos\theta)}}{|\vec{r}|-g\cos\theta}+\frac{e^{\mathrm{j}k(|\vec{r}|+g\cos\theta_I)}}{|\vec{r}|+g\cos\theta_I}\right)D_{LA}(\theta,\varphi,\Delta\psi) \tag{26}$$

The definitions of θ, φ and $\Delta\psi$ are the same as those presented in Eq. (24). The pressure field generated by a thin film suspended on a substrate can be directly obtained by replacing $D_{LA}(\theta,\varphi,\Delta\psi)$ with $D_f(\theta,\varphi)$.

2.5 Efficient input power

The efficient input power P_{in}^{e} is another key parameter to determine acoustic pressure fields. It is only part of the total input power to consider the heat loss and heat sink of TA devices. Indeed, the total input power consists of three parts, i.e., heat loss, heat sink into the devices and heat energy transferred into the surrounding medium. For a single line source, the heat loss, heat sink and heat transfer are, respectively, $2\pi r_0 l\beta_0 T_L$, $\pi r_0^2 l C_V \,\mathrm{d}T_L(t)/\mathrm{d}t$ and $-2\pi r_0 l\kappa\,\partial T(r)/\partial r\big|_{r=r_0}$, where r_0 is the radius of the line; C_V

is the heat capacity per unit volume; β_0 is the heat loss per unit area; and T_L is temperature of the line. As the temperature of waves attenuates sharply, it can only propagate in a short distance away from the line source. A cylindrical wave is suitable to simulate the temperature wave field $T(r)$. When the gap distance between the line source and the substrate is sufficiently large (larger than the thermal wavelength $\delta_g = 2\pi\sqrt{2\alpha/\omega}$), the cylindrical wave without considering the reflection effect from the substrate is always a good approximation. In another situation, if the gap distance cannot satisfy this requirement, the thermal wave can penetrate into the gas gap and a portion of heat energy will transfer to the substrate. As the heat conductivity of solid is typically prior to that of gas, the thermal wave that can be reflected from the solid-gas interface is usually very small. As a result, the thermal field distribution in the surrounding gas medium is insignificantly affected by the reflected wave. Hence, the thermal field can also be simulated by the cylindrical wave without considering the reflected wave from the substrate. Using the cylindrical thermal wave model proposed by Tong et al. [19] and following the conservation of energy, the efficient input power can be obtained as

$$P_{in}^{\ e} = \frac{2\lambda\kappa \mathrm{H}_1^{(1)}(\lambda r_0)}{\mathrm{H}_0^{(1)}(\lambda r_0)\cdot(2\beta_0 - j\omega C_V r_0) + 2\lambda\kappa \mathrm{H}_1^{(1)}(\lambda r_0)} P_{in}^{\ t} \tag{27}$$

where $P_{in}^{\ t}$ is the total input power and $H_i^{(1)}(\cdot)$ is the Bessel function.

A line array is considered as a thinfilm to obtain the efficient input power. Consider the strong attenuation, the thermal wave can only propagate within a short range. It can be viewed as a plane wave in the near-field region. The heat loss and heat sink for this situation are $2s\beta_0 T_f(t)$ and $sc_s\, dT_f(t)/dt$, respectively, in which $T_f(t)$, s and c_s are the temperature, area and HCPUA of the thinfilm, respectively. The temperature of the thinfilm can be calculated as [27]

$$T_f(t) = \frac{P_{in}^{\ e}}{s}\frac{1}{2\lambda\kappa}\left(1 + e^{-2\lambda g}\cdot\Re\right)\cdot \mathrm{e}^{-\mathrm{j}\omega t} \tag{28}$$

where $\Re = \left(2\sqrt{\alpha}\right)/\left(\kappa\sqrt{\alpha_s} + \kappa_s\sqrt{\alpha}\right)$ with α_s and κ_s the thermal diffusivity and conductivity of the substrate, respectively. The remaining heat energy is allocated to the surrounding gas for the generation of TA waves. As the plane wave is assumed, $\bar{T}_g(\vec{r}, g)$ can be obtained as follows [27]

$$T_g(\vec{r}, g) = \frac{P_{in}^{\ e}}{s}\frac{1}{2\lambda\kappa}\left[\Re\cdot e^{-\lambda(z+g)} + e^{-\lambda|z-g|}\right]\cdot \mathrm{e}^{-\mathrm{j}\omega t} \tag{29}$$

The heat energy transferred to the surrounding gas is $-\kappa\,\partial T_g(\vec{r}, g)/\partial z\big|_{z=g^-} + \kappa\,\partial T_g(\vec{r}, g)/\partial z\big|_{z=g^+}$. Based on the conservation of energy, we have

$$P_{in}^{\ t}\mathrm{e}^{-\mathrm{j}\omega t} = 2s\beta_0 T_f(t) + sc_s\frac{\mathrm{d}T_f(t)}{\mathrm{d}t} - \kappa\,\partial T_g(\vec{r}, g)/\partial z\big|_{z=g^-} + \kappa\,\partial T_g(\vec{r}, g)/\partial z\big|_{z=g^+} \tag{30}$$

in which the efficient input power is given by [27]

$$P_{in}^{\ e} = \frac{2\lambda\kappa P_{in}^{\ t}}{\left(2\beta_0 - \mathrm{j}\omega c_s\right)\left(1 + \Re e^{-2\lambda g}\right) - 2\mathrm{j}\lambda\kappa} \tag{31}$$

When the gap distance is sufficiently large, Eq. (31) can be further simplified as

$$P_{in}^{\ e} = \frac{2\lambda\kappa P_{in}^{\ t}}{2\beta_0 - j\omega c_s - 2j\lambda\kappa} \tag{32}$$

In Eq. (32), it is noted that the substrate does not contribute any effect on the efficient input power as the thermal wave has attenuated to a negligible level before it arrives at the substrate surface.

3. Results and discussion

A specific line array loudspeaker with aluminum wires suspended over a silicon substrate with a 5-μm air gap was designed [11]. The packing ratio is 1/10 with a line width of 3 μm and a thickness of 30 nm to minimize the HCPUA. The bulk dimension of this loudspeaker is 0.5 cm × 1 cm. For simplification, the length of all lines is assumed as 0.5 cm and the number of lines can be calculated as $n = 1\text{cm}/33\mu\text{m} \approx 333$. To estimate the efficient input power, the line array is approximately viewed as an aluminum thinfilm with a thickness of 30 nm and the corresponding HCPUA is 0.084 $Jm^{-2}K^{-1}$[32]. Because the total area of the line array is smaller than the equal-size thinfilm, less thermal energy can be absorbed by the line array. Therefore, the equivalent HCPUA is selected as 0.04 $Jm^{-2}K^{-1}$ in this work. As the heat loss is very small and does not contribute significant influence on the final pressure field, so this factor can be neglected. The thermal properties of air and silicon substrate are presented in Table 1.

The efficient input power and the acoustic pressure field can be obtained from Eqs. (26) and (31), respectively. In Fig. 4, the theoretical results of the acoustic pressure response in air are presented. Both on-axis and off-axis responses show good agreement with the available experimental results [11]. It is clear to observe the interference effect at the off-axis (20° and 40°) in both experimental and theoretical results. It is also found that the theoretical sound pressure level linearly increases with the logarithmic frequency on the axis. However, the measurement shows a flat frequency response when the frequency exceeds 100 kHz. The deviation of the theoretical prediction from the experimental measurement may be originated by neglecting the coupled term $-(\partial p/\partial t)/\kappa$ in Eq. (1) to obtain the thermal fields. Obviously, the magnitude of this term is proportional to the frequency. By increasing the response frequency, this term becomes dominant to cause the deviation between the theoretical prediction and the experimental results. The exact and approximate solutions to the thermal-mechanical coupled equations were proposed by Lim et al. [24] for a one-dimensional plane wave model. It is not difficult to verify that the approximate solution in the previous work [24] can be re-obtained by neglecting the coupled term $-(\partial p/\partial t)/\kappa$. Based on the detailed analysis (see Fig. 6 in Ref. [24]) on the approximate and exact solutions, the approximate solution deviates with the exact solution when the frequency exceeds 100 kHz. Unfortunately, the exact solution is difficult to directly obtain for a three-dimensional model, especially for the appearance of substrates. Therefore, the model proposed in this work is only suitable for a frequency range lower than 100 kHz.

In order to enforce the structure strength of TA devices, Wei and his associates [5] proposed a novel TA chip by suspending thin CNT yarns onto a patterned silicon wafer with an air gap between the yarns and the silicon wafer. A sound signal of 78 dB can be produced with an input power of 1W onto the CNT yarns at 10 kHz with a 150-μm gap distance. The bulk size of the device is estimated as $1.26\,\text{cm}\times 3\,\text{cm}$. The yarns are ~1 μm in diameter and 120 μm in pitch, implying that the number of yarns is $n = 3\,\text{cm}/120\,\mu\text{m} = 250$. The heat loss per unit area β_0 and the HCPUA of the CNT yarn array are, respectively, taken as 15 $\text{Wm}^{-2}\text{K}^{-1}$ and 0.12 $\text{Jm}^{-2}\text{K}^{-1}$ [27] to estimate the efficient input power P_{in}^{e}. Using Eq. (26), the variation of acoustic pressure responses at different frequencies and gap sizes is determined and presented in Fig. 5. Good agreement is observed between the present results and the experimental data. In Fig. 5 (a), it is shown that a larger gap distance can improve the performance of TA devices. The acoustic pressure response increases exponentially as the gap distance is smaller than $50\,\mu\text{m}$ as shown in Fig. 5 (c). To continuously increase the gap distance, the output acoustic pressure almost remains unchanged. For a small gap distance, the thermal wave can penetrate through air into the substrate. Consequently, a portion of the thermal energy will sink into the substrate and they do not have contribution to the acoustic pressure. By increasing the gap distance, less thermal energy can sink into the substrate to increase the acoustic pressure. When the gap distance exceeds a threshold value, the effect of the thermal energy on the substrate can be omitted. In Fig. 5 (b), the sound pressure level shows a logarithmic relationship with the frequency. The predicted pressure levels show a deviation from the experiment data at a high frequency in the $26\text{-}\mu\text{m}$ CNT yarn array device. It is possibly due to the under-estimation of heat loss, resulting in the over-estimation of the efficient input power for a small gap distance.

A linear power-dependent acoustic pressure is clearly seen in Fig. 6 (a). The comparison results verify again the accuracy of the proposed model in this work. The same device to that used in Fig. 5 is subject to different phased alternating current signals. The phased line array emission is shown in Fig. 6 (b). By applying a series of alternating current signals with a fixed phase shift, the principal maxima will shift with certain angles. The directivity and the interference lobes of the phased array acoustic radiation can also be clearly seen in Fig. 6 (b). Therefore, the CNT yarn array can be served as an acoustic radiation controller to manipulate the generation of acoustic signals in different directions with the supply of phased signals.

If a line space tends to be infinitesimal, the line array becomes a continuous thinfilm. Equation (25) can be used to investigate the pressure response of a thinfilm in a free-space. The heat loss coefficients β_0 for a single-layer and a four-layered CNT thinfilm are selected as 23 $\mathrm{WK^{-1}m^{-2}}$ and 27 $\mathrm{WK^{-1}m^{-2}}$, respectively [24]. The HCPUA of a single-layer CNT thinfilm is $7.7\times10^{-3}\,\mathrm{JK^{-1}m^{-2}}$ [6]. While the HCPUA of a four-layer CNT thinfilm can be estimated as four times of that of a single-layer CNT thinfilm. The on-axis frequency responses in air are shown in Figs. 7 (a) and 7 (b) for a single-layer ($3\,\mathrm{cm}\times3\,\mathrm{cm}$) and a four-layered CNT thinfilm ($3\,\mathrm{cm}\times3\,\mathrm{cm}$), respectively. The single-layer CNT thinfilm can generate a higher acoustic pressure than the four-layered CNT thinfilm under the same conditions, this is mainly due to the lower HCPUA of the single-layer CNT thinfilm. The off-axis pressure response for $\varphi=0^\circ$ at different frequencies is plotted in Fig. 7 (c). It is clear that the maximum pressure is at $\theta=0^\circ$. When the observation point is rotated with respect to the *y*-direction and it is kept at $\varphi=0^\circ$, no side lobe is observed at 10 kHz and only one side lobe is observed at

20 kHz. However, several side lobes can be found at 40 kHz due to the strong interference effect at high frequencies.

The off-axis pressure distribution with the angle φ generated by a four-layer CNT thinfilm at different frequencies and angles θ is presented in Fig. 8. As the frequency increases, the interference effect becomes more remarkable. When the pressure field is at a low frequency, no obvious effect is observed. The principle maxima and the side lobes appear as the response frequency increases due to the strong interference effect. In addition, the pattern of the pressure distribution is affected by the angle θ, because there are different interference patterns.

4. Conclusions

Acoustic pressure fields generated from a point source suspended over a substrate in a free-space and a half-space are studied theoretically. The analytical results can be directly applied to derive the acoustic pressure response of a thin line speaker using a mathematical integration technique. Further extension of the results of a thin line speaker to a thin yarn array, the acoustic pressure fields generated by the line array TA speaker in both free- and half-spaces are presented. By comparing with the available experimental results, the accuracy of the present analytical model is verified. It is found that the on-axis pressure fields are greatly different from the off-axis results. Strong interference effect is observed at the off-axis response and higher frequencies can strengthen the interference effect. For a suspended thin line array on a substrate, the gap distance between the array and the substrate is a dominant factor. A larger gap distance can enhance the performance efficiency of the thin line array TA devices. When the gap distance is out of the threshold value, there is no significant effect on the pressure field. Although the examples presented herein focus on the acoustic pressure responses in air, it is easy to extend the present work in other media (e.g., argon and helium) by replacing the thermal parameters of air with those of the corresponding media. The present model is well validated with the available experimental data. It can be extended to investigate TA pressure responses generated by arbitrary sources, and also can provide effective guidelines for design and optimization of thin line array TA devices.

Acknowledgements

The work described in this paper was supported by Natural Science Foundation of Jiangxi (20171BAB216047) and National Natural Science Foundation of China (Grant Nos. 11702095 and 11602210). The Early Career Scheme from the Research Grants Council of the Hong Kong Special Administrative Region (Project No. PolyU 252026/16E) is also gratefully acknowledged.

References

[1] R. Venkatasubramanian, Applied physics: Nanothermal trumpets, Nature, 463 (2010) 619-619.

[2] H.D. Arnold, I.B. Crandall, The Thermophone as a Precision Source of Sound, Physical Review, 10 (1917) 22-38.

[3] H.N. Shinoda, T.; Ueno, K.; Koshida, N., Thermally induced ultrasonic emission from porous silicon, Nature, 400 (1999) 853-855.

[4] L.H. Tong, S.K. Lai, C.W. Lim, Broadband signal response of thermo-acoustic devices and its applications, The Journal of the Acoustical Society of America, 141 (2017) 2430–2439.

[5] Y. Wei, X.Y. Lin, K.L. Jiang, P. Liu, Q.Q. Li, S.S. Fan, Thermoacoustic Chips with Carbon Nanotube Thin Yarn Arrays, Nano Letters, 13 (2013) 4795-4801.

[6] L. Xiao, Z. Chen, C. Feng, L. Liu, Z.-Q. Bai, Y. Wang, L. Qian, Y. Zhang, Q. Li, K. Jiang, S. Fan, Flexible, Stretchable, Transparent Carbon Nanotube Thin Film Loudspeakers, Nano Letters, 8 (2008) 4539-4545.

[7] Z.C. Wu, Z.H. Chen, X. Du, J.M. Logan, J. Sippel, M. Nikolou, K. Kamaras, J.R. Reynolds, D.B. Tanner, A.F. Hebard, A.G. Rinzler, Transparent, conductive carbon nanotube films, Science, 305 (2004) 1273-1276.

[8] M. Zhang, S.L. Fang, A.A. Zakhidov, S.B. Lee, A.E. Aliev, C.D. Williams, K.R. Atkinson, R.H. Baughman, Strong, transparent, multifunctional, carbon nanotube sheets, Science, 309 (2005) 1215-1219.

[9] M.E. Kozlov, C.S. Haines, J.Y. Oh, M.D. Lima, S.L. Fang, Sound of carbon nanotube assemblies, Journal of Applied Physics, 106 (2009).

[10] A.O. Niskanen, J. Hassel, M. Tikander, P. Maijala, L. Gronberg, P. Helisto, Suspended metal wire array as a thermoacoustic sound source, Appl Phys Lett, 95 (2009).

[11] V. Vesterinen, A.O. Niskanen, J. Hassel, P. Helistö, Fundamental Efficiency of Nanothermophones: Modeling and Experiments, Nano Letters, 10 (2010) 5020-5024.

[12] H. Tian, D. Xie, Y. Yang, T.L. Ren, Y.X. Lin, Y. Chen, Y.F. Wang, C.J. Zhou, P.G. Peng, L.G. Wang, L.T. Liu, Flexible, ultrathin, and transparent sound-emitting devices using silver nanowires film, Appl Phys Lett, 99 (2011).

[13] G. Chitnis, A. Kim, S.H. Song, A.M. Jessop, J.S. Bolton, B. Ziaie, A thermophone on porous polymeric substrate, Appl Phys Lett, 101 (2012) 021911-021914.

[14] N. Koshida, D. Hippo, M. Mori, H. Yanazawa, H. Shinoda, T. Shimada, Characteristics of thermally induced acoustic emission from nanoporous silicon device under full digital operation, Appl Phys Lett, 102 (2013).

[15] H. Tian, T.-L. Ren, D. Xie, Y.-F. Wang, C.-J. Zhou, T.-T. Feng, D. Fu, Y. Yang, P.-G. Peng, L.-G. Wang, L.-T. Liu, Graphene-on-Paper Sound Source Devices, ACS Nano, 5 (2011) 4878-4885.

[16] B.R. Dzikowicz, J.F. Tressler, J.W. Baldwin, Cylindrical heat conduction and structural acoustic models for enclosed fiber array thermophones, J Acoust Soc Am, 142 (2017) 3187-3197.

[17] A.E. Aliev, S. Perananthan, J.P. Ferraris, Carbonized Electrospun Nanofiber Sheets for Thermophones, ACS Applied Materials & Interfaces, 8 (2016) 31192-31201.

[18] B.J. Mason, S.W. Chang, J.H. Chen, S.B. Cronin, A.W. Bushmaker, Thermoacoustic Transduction in Individual Suspended Carbon Nanotubes, Acs Nano, 9 (2015) 5372-5376.

[19] L.H. Tong, C.W. Lim, X.S. Zhao, D.X. Geng, Theory and modeling of cylindrical thermo-acoustic transduction, Phys Lett A, 380 (2016) 2123-2128.

[20] A.E. Aliev, M.D. Lima, S. Fang, R.H. Baughman, Underwater Sound Generation Using Carbon Nanotube Projectors, Nano Letters, 10 (2010) 2374-2380.

[21] L. Xiao, P. Liu, L. Liu, Q. Li, Z. Feng, S. Fan, K. Jiang, High frequency response of carbon nanotube thin film speaker in gases, Journal of Applied Physics, 110 (2011) 084311-084315.

[22] A.E. Aliev, Y.N. Gartstein, R.H. Baughman, Increasing the efficiency of thermoacoustic carbon nanotube sound projectors, Nanotechnology, 24 (2013).

[23] H. Hu, T. Zhu, J. Xu, Model for thermoacoustic emission from solids, Appl Phys Lett, 96 (2010) 214101-214103.

[24] C.W. Lim, L.H. Tong, Y.C. Li, Theory of suspended carbon nanotube thinfilm as a thermal-acoustic source, Journal of Sound and Vibration, 332 (2013) 5451-5461.

[25] S.S. Asadzadeh, A. Moosavi, C. Huynh, O. Saleki, Thermo acoustic study of carbon nanotubes in near and far field: Theory, simulation, and experiment, Journal of Applied Physics, 117 (2015) 095101.

[26] L.H. Tong, C.W. Lim, Y.C. Li, Gas-Filled Encapsulated Thermal-Acoustic Transducer, J Vib Acoust, 135 (2013).

[27] L.H. Tong, C.W. Lim, S.K. Lai, Y.C. Li, Gap separation effect on thermoacoustic wave generation by heated suspended CNT nano-thinfilm, Appl Therm Eng, 86 (2015) 135-142.

[28] M. Asgarisabet, A. Barnard, Multi-Physics Simulation of Ultra-Lightweight Carbon Nanotube Speakers, 10 (2017).

[29] L.L. Beranek, T. Mellow, Acoustics: Sound Fields and Transducers, 1st ed., Academic Press, 2012.

[30] K.T. Tang, Mathematical Methods for Engineers and Scientists 3: Fourier Analysis, Partial Differential Equations and Variational Methods, Springer, 2007.

[31] M. Ochmann, The complex equivalent source method for sound propagation over an impedance plane, J Acoust Soc Am, 116 (2004) 3304-3311.

[32] V. Vesterinen, A.O. Niskanen, J. Hassel, P. Helistö, Fundamental Efficiency of Nanothermophones: Modeling and Experiments. Auxiliary Material, Nano Letters, 10 (2010).

[33] L.E. Kinsler, A.R. Frey, A.B. Coppens, J.V. Sanders, Fundamentals of Acoustics, 4th ed., Wiley, 1999.

Table caption

Table 1 Thermal properties of air and substrate at 300 K.

Figure captions

Fig. 1 (a) Schematic diagram of a thin line array TA device; and (b) its side view.

Fig. 2 Coordinate arrangement for pressure fields generated by a line source in (a) a free-space; and (b) a half-space with the line source suspended over a substrate. Note that when the observation point P is in the space y < 0, the angle θ is a negative value.

Fig. 3 Coordinate arrangement of a line array in (a) a free-space; and (b) a half-space with the line array suspended over a substrate.

Fig. 4 Pressure fields generated by an aluminum line array speaker at different input frequencies. The observation distance is r = 17 cm and the total input power is 1.2 W. The off-axis responses for $\varphi = 0^\circ$ at $\theta = 20^\circ$ and $\theta = 40^\circ$ are also presented for comparison. The air gap is $5\,\mu\text{m}$. No initial phase difference $\Delta\psi$ is set for this case.

Fig. 5 (a) Theoretical prediction of acoustic pressure responses for a CNT yarn line array device; (b) Effect of frequency on the acoustic pressure level at different gap sizes; and (c) Effect of gap distance on acoustic pressure at different frequencies. Lines denoted by capital letters A to D in Figs. 5 (b) and 5 (c) correspond to those in Fig. 5 (a). The observation point is located at r = 5 cm on the center axis and the total input power is 1W. No initial phase difference $\Delta\psi$ is set.

Fig. 6 (a) Comparison of power-dependent pressure responses generated by a CNT yarn array; (b) Simulation of phased line array emission at $\varphi = 0^\circ$. The array used is the same to that in Fig. 5. The observation point is r = 5 cm and the gap distance is $150\,\mu\text{m}$ both in Figs. 6 (a) and 6 (b). The total input power in Fig. 6 (b) is 1W and the corresponding frequency is 40 kHz. The phase shift 2.5° means that the n^{th} line has a phase shift 2.5 (n-1)° with respect to the first line.

Fig. 7 Frequency response for (a) a single-layer CNT thinfilm; (b) a four-layer CNT thinfilm; and (c) theoretical prediction of the off-axis pressure responses at $\varphi = 0^\circ$ for different frequencies. The total input power in Fig. 7 (a) and 7 (b) is 4.5 W while is 1 W in Fig. 7 (c). All the observation points are set at r = 5 cm.

Fig. 8 Theoretical prediction for the off-axis pressure fields generated by a four-layer CNT thinfilm at (a) 10 kHz; (b) 20 kHz; (c) 40 kHz; and (d) 60 kHz. The total input power for each case is 1 W and all the observation points are set at r = 5 cm.

Table 1 Thermal properties of air and substrate at 300 K.

	α ($mm^2 s^{-1}$)	κ ($W\,m^{-1}K^{-1}$)	C_V ($J\,m^{-3}K^{-1}$)	C_0 (ms^{-1})	ρ ($kg\,m^{-3}$)
Air [29]	22.5	0.0263	-	344	1.16
Silicon [29]	9.588×10^{-5}	160	1.66×10^{6}	-	-

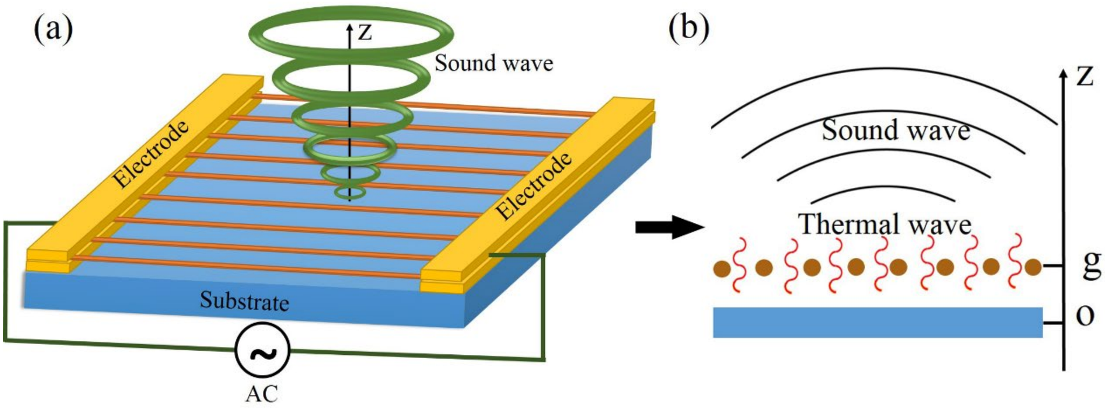

Fig. 1 (a) Schematic diagram of a thin line array TA device; and (b) its side view.

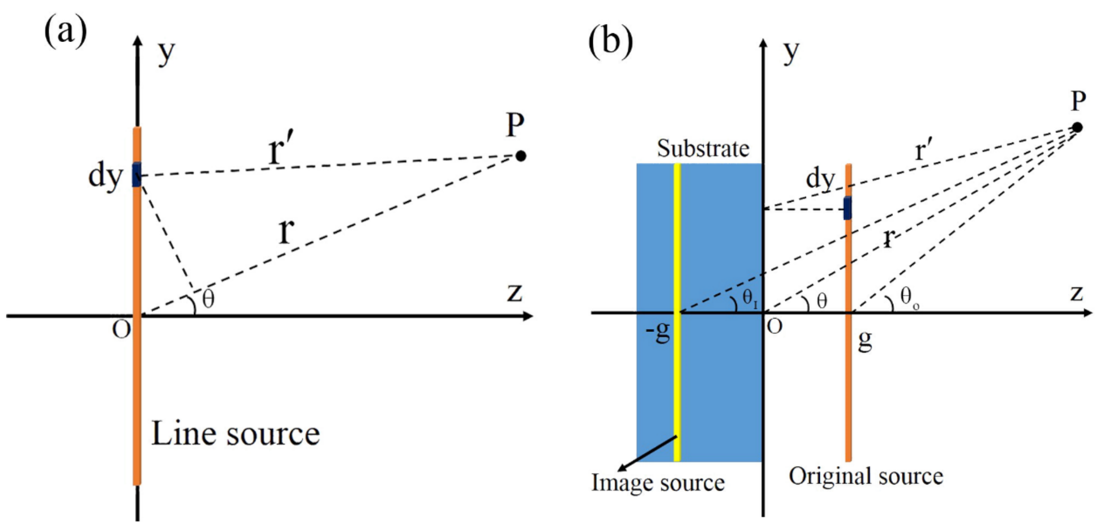

Fig. 2 Coordinate arrangement for pressure fields generated by a line source in (a) a free-space; and (b) a half-space with the line source suspended over a substrate. Note that when the observation point P is in the space y < 0, the angle θ is a negative value.

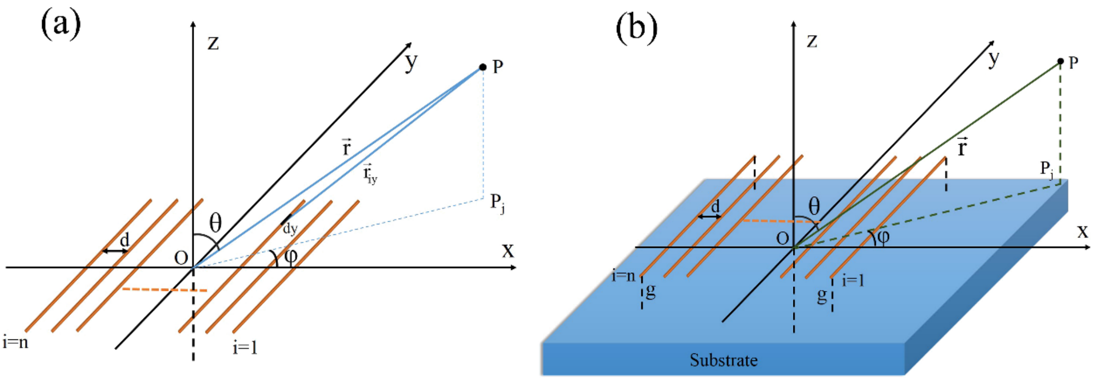

Fig. 3 Coordinate arrangement of a line array in (a) a free-space; and (b) a half-space with the line array suspended over a substrate.

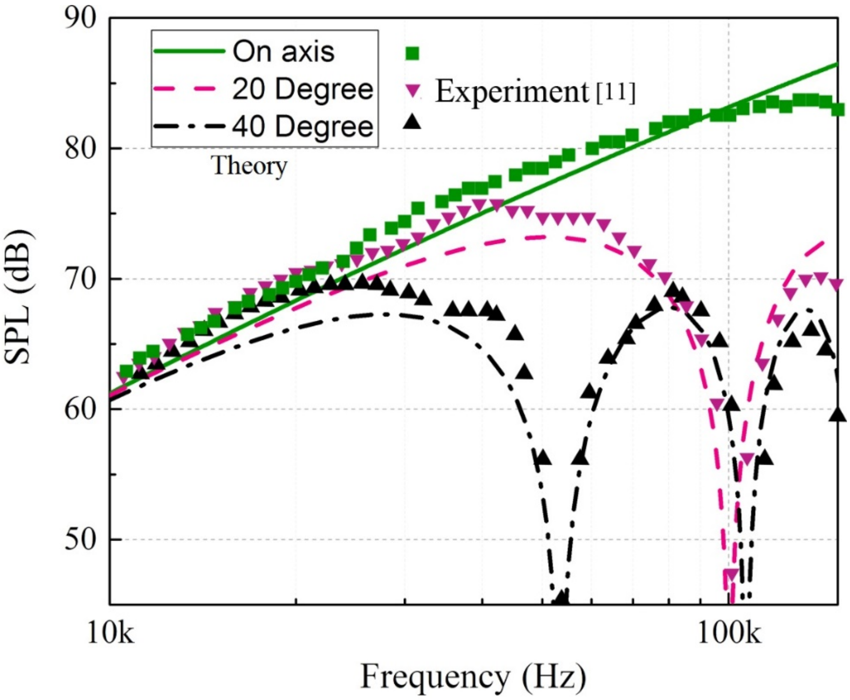

Fig. 4 Pressure fields generated by an aluminum line array speaker at different input frequencies. The observation distance is r = 17 cm and the total input power is 1.2 W. The off-axis responses for $\varphi = 0^{\circ}$ at $\theta = 20^{\circ}$ and $\theta = 40^{\circ}$ are also presented for comparison. The air gap is $5\,\mu\text{m}$. No initial phase difference $\Delta\psi$ is set for this case.

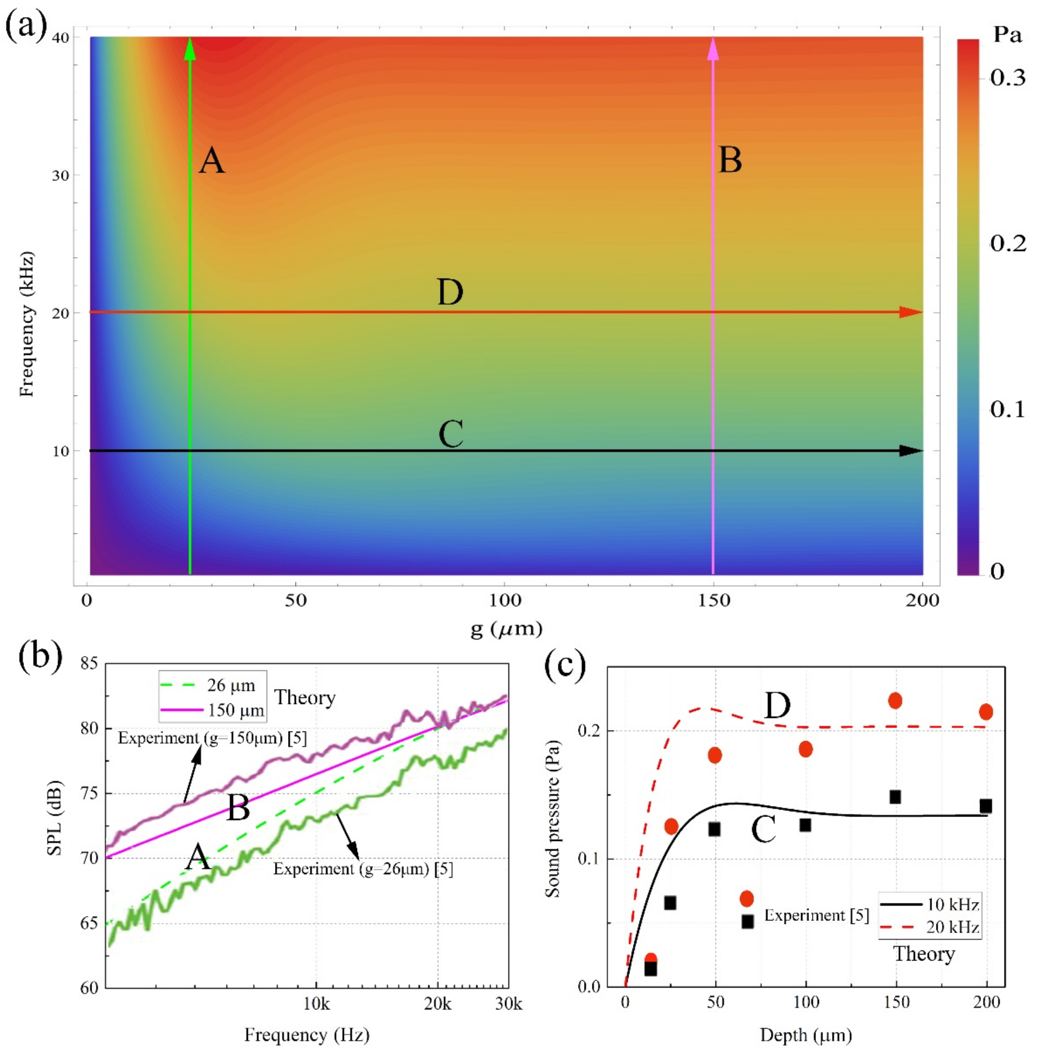

Fig. 5 (a) Theoretical prediction of acoustic pressure responses for a CNT yarn line array device; (b) Effect of frequency on the acoustic pressure level at different gap sizes; and (c) Effect of gap distance on acoustic pressure at different frequencies. Lines denoted by the capital letters A to D in Figs. 5 (b) and 5 (c) correspond to those in Fig. 5 (a). The observation point is located at r = 5 cm on the center axis and the total input power is 1W. No initial phase difference $\Delta\psi$ is set.

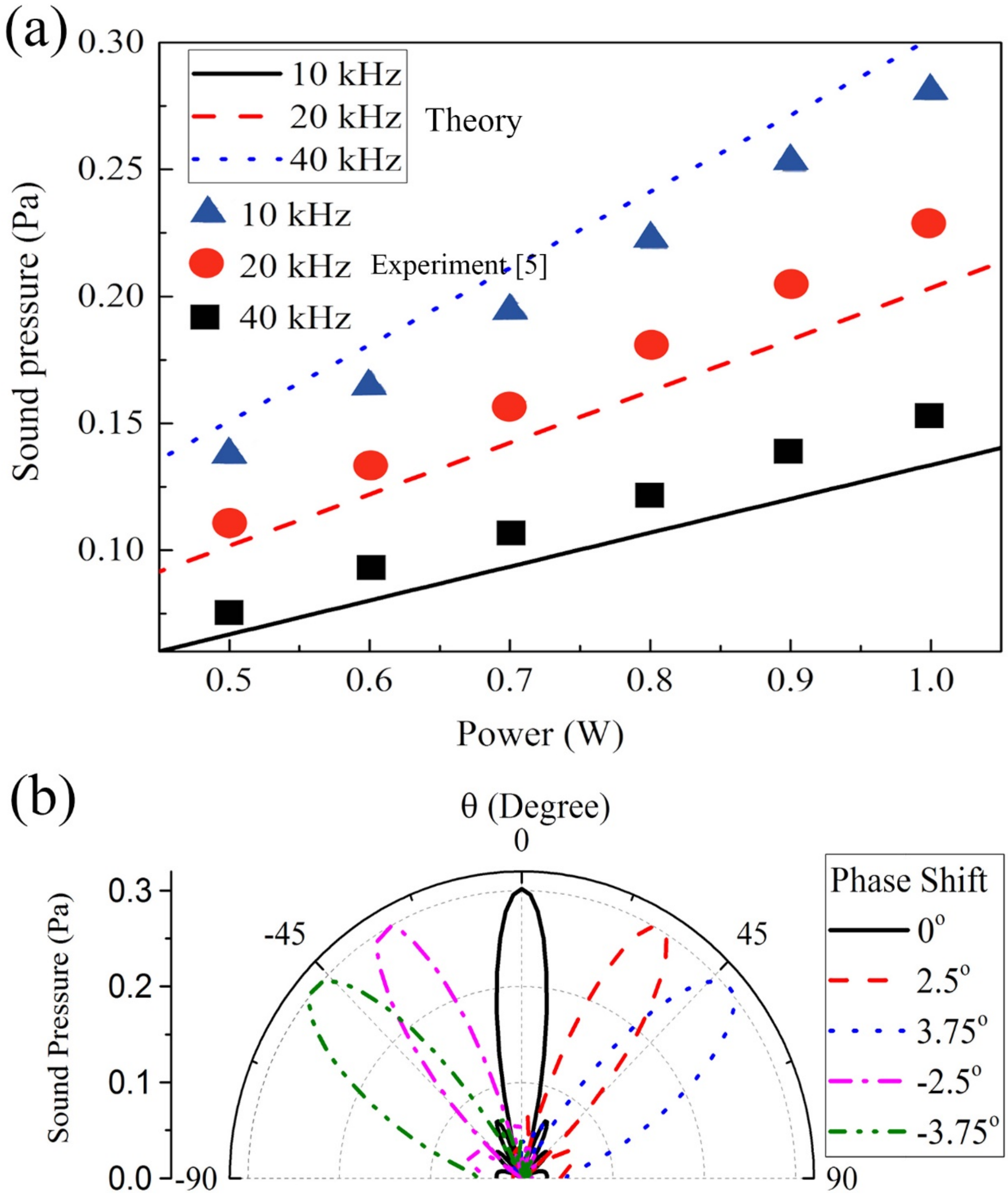

Fig. 6 (a) Comparison of power-dependent pressure responses generated by a CNT yarn array; (b) Simulation of phased line array emission at $\varphi = 0^\circ$. The array used is the same to that in Fig. 5. The observation point is r = 5 cm and the gap distance is 150 μm both in Figs. 6 (a) and 6 (b). The total input power in Fig. 6 (b) is 1W and the corresponding frequency is 40 kHz. The phase shift 2.5° means that the n^{th} line has a phase shift 2.5 (n-1)° with respect to the first line.

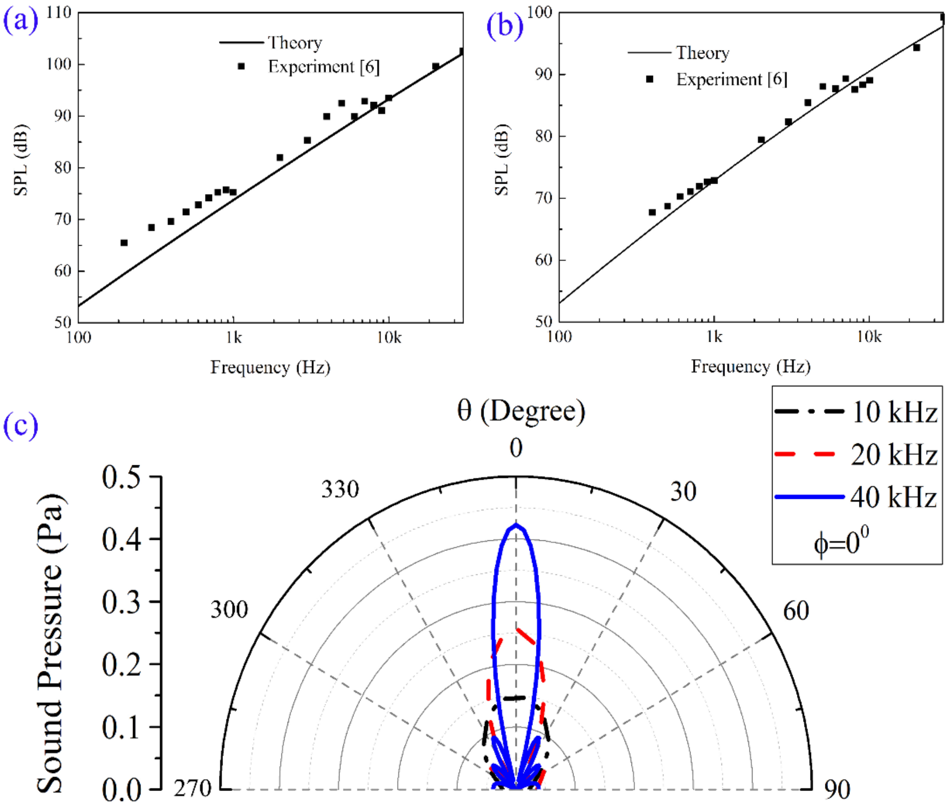

Fig. 7 Frequency response for (a) a single-layer CNT thinfilm; (b) a four-layer CNT thinfilm; and (c) theoretical prediction of the off-axis pressure responses at $\varphi = 0^{\circ}$ for different frequencies. The total input power in Fig. 7 (a) and 7 (b) is 4.5 W while is 1 W in Fig. 7 (c). All the observation points are set at r = 5 cm.

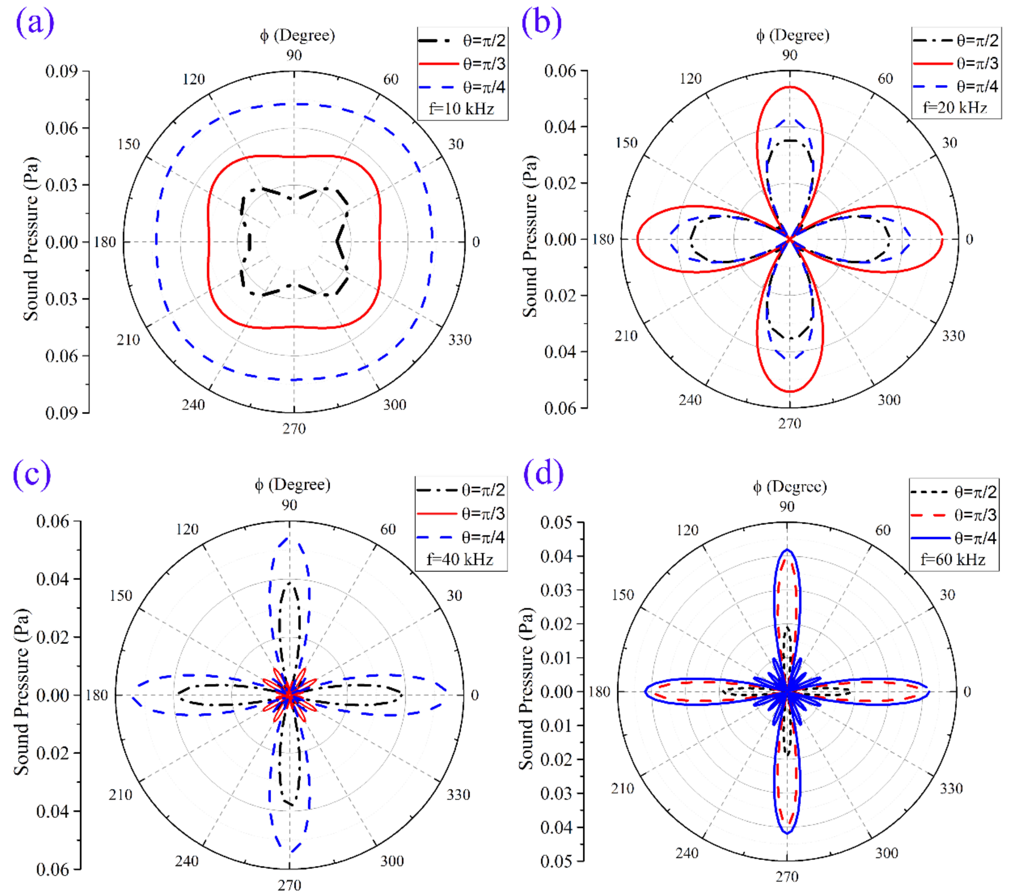

Fig. 8 Theoretical prediction for the off-axis pressure fields generated by a four-layer CNT thinfilm at (a) 10 kHz; (b) 20 kHz; (c) 40 kHz; and (d) 60 kHz. The total input power for each case is 1 W and all the observation points are set at r = 5 cm.